International Journal of Technology v(i) pp-pp (YYYY)
Received Month Year / Revised Month Year / Accepted Month Year

International Journal of Technology

http://ijtech.eng.ui.ac.id

Magnetic Nanocomposite of Hydroxyapatite/Co doped $ZnFe_2O_4$ Synthesized by Green Technology: Structure, Character, and Its Application

Abstract. This study aimed to create hydroxyapatite/Co-doped-$ZnFe_2O_4$ with a mole ratio of Co:Zn of 0.1:0.9 ($HA/Co_{0.1}Zn_{0.9}Fe_2O_4$) nanocomposites by a hydrothermal method using waste from Pensi clam shells as a calcium source for the synthesis of hydroxyapatite. The nanocomposites were applied to remediate organic contaminants and metal ions in water. Various characterization techniques confirmed the successful fabrication of $HA/Co_{0.1}Zn_{0.9}Fe_2O_4$ magnetic nanocomposite. XRD pattern revealed distinct peaks indicating the formation of the nanocomposite, and no impurities were observed. FTIR analysis shows the absorption bands at wave numbers 482 cm^{-1} and 534 cm^{-1}, signifying the existence of M-O vibrations for the octahedral and tetrahedral sides of the ferrite contained in the nanocomposite. The nanocomposites exhibit superparamagnetic behavior, with a saturation magnetization ranging from 0.64 to 2.047 emu/g. The energy gap values in the visible light spectrum are between 2.25 and 2.4 eV. The BET method was employed to ascertain the specific surface area of the nanocomposites, producing 32.01 m^2/g for those with a HA: $Co_{0.1}Zn_{0.9}Fe_2O_4$ ratio of 16:4. The composite exhibited 92.51% Cd(II) metal ions adsorption and 98.65% dye degradation. These magnetic nanocomposites have the potential to serve as an efficient and environmentally friendly sorbent for Cd(II) ions and as a catalyst for wastewater dye degradation.

Keywords: Green Technology; $HA/Co_{0.1}Zn_{0.9}Fe_2O_4$; Pensi calm shells; Photocatalyst, Superparamagnetic;

1. Introduction

Industrial waste is progressively emerging as a significant source of water pollution. Various industries contaminate water, including printing, textiles, chemicals, electronics, pharmaceuticals, and machinery manufacturing. The chemicals, electronics, and pharmaceutical sectors are heavily involved in this issue (Desalegn et al., 2020). They caused many contaminants, such as dyes, heavy metals, phenols, herbicides, insecticides, and medications, to leak into the aquatic environment as byproducts without being adequately treated (Elgarahy et al., 2021). These pollutants pose significant dangers to human health and aquatic organisms (Tamjidi et al., 2019). Many widely used techniques, including coagulation, membrane processes, activated carbon adsorption, ozonation, adsorption, microbial breakdown, and electrochemical removal, have been employed to address the issue of water environmental pollution (Handayani et al., 2024; Madkhali et al., 2023; Karamah et al., 2019). The major limitations of each method include the difficulty in sludge formation, high chemical usage, increased operational costs, and the potential transfer of pollutants between stages. Environmentalists and researchers have recently become interested in wastewater pollution caused by dyes and heavy metal ions (Kartika et al., 2023), as it is a severe environmental concern in both developed and developing countries. Various synthesized materials have been utilized to diminish the environmental impacts of water pollutants. This includes the use of catalysts to degrade dyes and adsorbent materials to extract metal ions (Rahmayeni et al., 2023). Hernández employed

Eichhornia crassipes as an adsorbent to eliminate methyl orange and methylene blue from residual solutions (Hernández et al., 2022). Yue et al. synthesized a cellulose-based adsorbent designed for the removal of both anionic and cationic dyes (Yue et al., 2019). Ubando et al. have explored microalgae as a viable and sustainable biosorbent for the removal of heavy metals in wastewater treatment processes (Ubando et al., 2021).

Hydroxyapatite, with the molecular formula $Ca_{10}(PO_4)_6(OH)_2$, possesses excellent biocompatibility and bioactivity, along with a high adsorption capacity and a large surface area, making it suitable for both dye removal and metal ion adsorption. (Supriyono et al., 2023). Because it is more affordable and natural, made from natural materials like bone, limestone, and shells, hydroxyapatite is the preferable material for some purposes such as for dental implants, drug delivery, cosmetics, etc. (Rimus et al., 2024; Supriyono et al., 2023). However, due to its difficulty separating from the liquid, utilizing hydroxyapatite alone is less economical. Therefore, it is necessary to modify hydroxyapatite to work more optimally, adsorb dyes in the visible light area and can be separated from the liquid. Then, it can be reused to make the following process more efficient. Combining spinel ferrite nanoparticles (MFe_2O_4) with hydroxyapatite is a viable option (Sery et al., 2021).

Recently, ferrite spinel-based materials and their composites have been extensively studied and used as water dye degradation catalysts. Spinel ferrites featuring one metallic ion in the formula $M(II)Fe_2O_4$ such as $CoFe_2O_4$, $NiFe_2O_4$, $CuFe_2O_4$, and $ZnFe_2O_4$, exhibit remarkable magnetic properties (Ganesan et al., 2024; Rahmayeni et al., 2021). At the nanoscale, these spinel ferrites demonstrated exceptional physical and chemical characteristics which renders them suitable for a range of applications, such as supercapacitors, semiconductors, catalysts, and cathode for olid oxide fuel cells (Fatah et al., 2023). Combining spinel ferrite (MFe_2O_4) compounds with hydroxyapatite creates composites that have improved characteristics over their original form. Nanocomposites of spinel ferrite with hydroxyapatite have been synthesized by many researchers. A novel magnetic $Zn/HAP/MgFe_2O_4$ nanocomposite was effectively produced in three stages and employed as a catalyst for the degradation of malachite green dye (Das and Dhar, 2020). A zinc ferrite nanocomposite encapsulated in hydroxyapatite was synthesized for the removal of cadmium (II) from aqueous solutions. The results demonstrated that the composite could eliminate 89.6% of Cd(II) ions from the solutions under optimal reaction conditions (Das and Dhar, 2020). A novel magnetic nanocomposite, featuring Sn(II)-incorporated hydroxyapatite (HAp) embedded in nickel ferrite ($NiFe_2O_4$@-HAp-Sn^{2+}), has been successfully produced using a simple method. The nanocomposite displayed exceptional photocatalytic efficiency in removing rhodamine B dye (Das et al., 2021). A bentonite/$CoFe_2O_4$/hydroxyapatite composite has been created for the purpose of adsorbing Pb(II) from wastewater. (Desalegn et al., 2020). Zinc ferrite/hydroxyapatite ceramic with nano-sized grains was fabricated through a solid-state reaction process using chicken eggshells were chosen to be calcium source for synthesizing HAp had been conducted by. The research on the $CuFe_2O_4$@hydroxyapatite composite for the environmental remediation of certain heavy metal ions was also carried out by (Sery et al., 2021; Ibrahim 2020).

$ZnFe_2O_4$ is one of the spinel ferrite materials that could be mixed with hydroxyapatite. These nanoparticles are stable spinel ferrite materials with low magnetic properties. Doping spinel ferrite with metal ions such as cobalt and others can significantly improve its magnetic properties. According to Padhan et al. (2019), doping spinel ferrite with metal elements could improve its magnetic characteristics, enabling it to be more strongly attracted to external magnetic fields (Padhan et al., 2023). Gómez et al. synthesized Co^{2+} doped $ZnFe_2O_4$ with ratios ranging from x = 0.0 to 1.0 using the co-precipitation method.

Introducing Co^{2+} doping at a ratio of x = 0.1 enhanced the magnetic properties of $ZnFe_2O_4$, transitioning it from paramagnetic to superparamagnetic (Gómez- et al., 2018). In this study, a green synthesis approach was introduced to create a nanocomposite consisting of hydroxyapatite and Co-doped $ZnFe_2O_4$ with a mole ratio of Co:Zn of 0.1:0.9 ($HA/Co_{0.1}Zn_{0.9}Fe_2O_4$). The food waste of Pensi clam shells (*Corbicula moltkiana*) utilized as a calcium carbonate source for hydroxyapatite synthesis. These Pensi clam shells were collected from Lake Singkarak in West Sumatra. Their high calcium content makes them a viable calcium oxide source for producing hydroxyapatite (Panda et al., 2021). The nanocomposites were synthesized using the hydrothermal method due to simplicity of synthesis with gambir leaf extract as the medium. This extract, abundant in secondary metabolite compounds, acts as a capping agent (Labanni et al., 2019). These compounds prevent particle agglomeration by regulating particle growth and reducing the particles' surface energy (Rahmayeni et al., 2022; Javed et al., 2020). It is expected that the resulting nanocomposites could function as an adsorbent and photocatalyst. The ability of the $HA/Co_{0.1}Zn_{0.9}Fe_2O_4$ nanocomposites to adsorb Cd (II) metal ions in water was determined. The heavy metal ion Cd (II) in water is often produced from automotive and battery waste (Lei et al., 2019). The photocatalytic performance of the synthesized nanocomposites was analyzed by evaluating their capacity to degrade direct red 81 dye. Direct red 81 ($C_{29}H_{19}N_5Na_2O_8S_2$), commonly found in textile industry wastewater, is notoriously difficult to decompose naturally (Hassaan et al., 2022; Dehghani et al., 2018). Various parameters related to photocatalytic and adsorption processes were investigated in this study. This involved determining the optimal catalyst amount, contact time, and concentrations of dyes or metal ions to evaluate the remediation efficiency of the synthesized nanocomposite in removing dyes and metal ions from wastewater.

2. Methods

2.1. Materials

The materials used in this study were purchased from Merck and included $CdCl_2.H_2O$, $(NH_4)_2HPO_4$, HNO_3, $Zn(NO_3)_2.4H_2O$, $Co(NO_3)_2.6H_2O$, $Fe(NO_3)_3.9H_2O$ and NaOH. Additionally, deionized water and NH_4OH were employed. Direct Red 81 ($C_{29}H_{19}N_5Na_2O_8S_2$) served as the model dye for the experiments obtained from a textile factory in West Sumatra. Pensi (*Corbicula molkiana*) clam shells were collected from Lake Singkarak in West Sumatra, Indonesia, while gambir leaves were sourced from the agricultural fields of the Faculty of Agriculture at Andalas University.

2.2. Extraction process of gambir leaf

Leaves of Gambir (*Uncaria gambir* Roxb.) were collected from the experimental garden located at the Faculty of Agriculture, Andalas University. The fresh leaves were carefully washed several times to eliminate dust and impurities. They were then shade-dried at room temperature for about five days. Once fully dried, the leaves were ground into a fine powder using a grinder and stored in a sterile container. For the extract preparation, 10 grams of gambir leaf powder were combined with one hundred millilitres of distilled water and stirred at 60°C for two hours. After stirring, the solution was filtered, and the resulting filtrate was kept in a refrigerator until it was needed for the synthesis of nanocomposites. (Labanni et al., 2019).

2.3. Synthesis of hydroxyapatite (HA) from Pensi clam shells

Pensi (*Corbicula moltkiana*) clam shells were collected from Singkarak Lake in West Sumatera and processed according to methods established by previous researchers. Initially, the shells were washed with water and dried at 110°C. They were then ground into a fine powder using a Fritsch Pulverisette 16 grinder. The powder was subsequently calcined at 900°C for five hours to produce calcium oxide (CaO). X-ray fluorescence analysis was carried out to evaluate the elemental composition of the Pensi clam shells. The extracted CaO was used as a precursor to produce hydroxyapatite. The procedure used in the previous study was modified to synthesize hydroxyapatite. A total of 4.2 grams of finely calcined calcium oxide (CaO) powder, obtained from Pensi clam shells, was dissolved in 75 mL of 2M nitric acid (HNO3). The resulting solution was stirred at 85°C and then filtered. Subsequently, 250 mL of 0.18 M ammonium hydrogen phosphate ($(NH_4)_2HPO_4$) was added to the mixture in a dropwise manner, while it was agitated at a speed of 500 rpm and maintained at a temperature of 110°C. The pH of the solution was raised to 11 by adding NH_4OH, and the mixture was constantly agitated for five hours. The precipitate and filtrate were separated after letting the produced white sol settle for the following day. After that, the powder was heated fo r 5 hours at 110°C in an oven and then calcined for 3 hours at 800°C. The obtained hydroxyapatite sample was characterized using a variety of techniques. The following equations represent the theoretical reactions involved in the synthesis of hydroxyapatite (Rahmayeni et al., 2023; Labani et al., 2020).

$$CaCO_3 \rightarrow CaO + CO_2 \quad (1)$$

$$CaO + 2HNO_3 \rightarrow Ca(NO_3)_2 + H_2O \quad (2)$$

$$10Ca(NO_3)_2 + 6(NH_4)_3PO_4 + 2NH_4OH \rightarrow Ca_{10}(PO_4)_6(OH)_2 + 20NH_4NO_3 \quad (3)$$

2.4. Synthesis of Co-doped $ZnFe_2O_4$ with a mole ratio of Co:Zn of 0.1:0.9 ($Co_{0.1}Zn_{0.9}Fe_2O_4$)

The $Co_{0.1}Zn_{0.9}Fe_2O_4$ nanoparticles were synthesized via the hydrothermal method using gambir leaf extract as a capping agent. For the synthesis, 8.079 g of $Fe(NO_3)_3 \cdot 9H_2O$, 2.353 g of $Zn(NO_3)_2 \cdot 6H_2O$, and 0.291 g of $Co(NO_3)_2$ were dissolved in 40 mL of a mixture comprising distilled water and gambir leaf extract in a 35:5 mL ratio. This solution was stirred at 500 rpm using a magnetic stirrer for 1 hour, after which 2M NaOH was added to adjust the pH to 12. The resulting suspension was placed in an autoclave and heated at 180°C for 3 hours. The precipitate was filtered, washed with distilled water until the pH became neutral, dried at 110°C for 3 hours, and then ground to a fine powder. The obtained $Co_{0.1}Zn_{0.9}Fe_2O_4$ powder was characterized using various instruments and subsequently employed in the synthesis of nanocomposites (Rahmayeni et al., 2023).

2.5. Synthesis of HA/$Co_{0.1}Zn_{0.9}Fe_2O_4$

The HA/$Co_{0.1}Zn_{0.9}Fe_2O_4$ nanocomposites were synthesized using the hydrothermal method. The procedure is as follows: First, HA and $Co_{0.1}Zn_{0.9}Fe_2O_4$ were mixed with a mole ratio of Co and Zn (0.1: 0.9) in 40 mL of gambir leaf extract and distilled water with a ratio of 5:35. The mixture was stirred until homogeneous for 30 minutes, then the pH was adjusted to 12 by adding 2 M NaOH. The mixture's temperature was maintained in the range of 70 ºC – 80 ºC. After that, the formed suspension was heated at 180°C for 3 hours in an autoclave, and the formed brown precipitate was filtered and washed using distilled water to a pH of 7. Furthermore, the precipitate was calcined at 400°C for 4 h. After that, the obtained powder was dried at 110°C for 3 h, then crushed until smooth. The nanocomposite product was labeled as CoZnHA (Rahmayeni et al., 2023). The ratio effect of HA: $Co_{0.1}Zn_{0.9}Fe_2O_4$ was studied by synthesizing the nanocomposite material into four variations based on the mass ratio of HA in HA/$Co_{0.1}Zn_{0.9}Fe_2O_4$ nanocomposites, as shown

in Table 1. The proposed synthesis mechanism of nanocomposite is represented in Figure S1.

Table 1 Comparison of HA: $Co_{0.1}Zn_{0.9}Fe_2O_4$ and sample names.

Comparison of HA : $Co_{0.1}Zn_{0.9}Fe_2O_4$ (g)	Sample names CoZnHA
19 : 1	CoZnHA1
18 : 2	CoZnHA2
17 : 3	CoZnHA3
16 : 4	CoZnHA4

2.6. Characterization of samples

The synthesized samples were characterized using various analytical techniques. X-ray diffraction (XRD: PANalytical MPD PW3040/60) with Cu Kα radiation in the range of 10-80° was employed to determine the crystal structure. The morphology and elemental composition were examined using Scanning Electron Microscopy coupled with Energy Dispersive X-ray Spectroscopy (SEM-EDX: HITACHI FLEXSEM 100). Fourier Transform Infrared Spectroscopy (FTIR: Subtech Spectrum ACII PEDS 4.00) was utilized to identify the interactions within the sample, with a wavenumber range of 200-4000 cm^{-1}. The magnetic properties were assessed using a Vibrating Sample Magnetometer (VSM, model VSM250). To analyze the absorption region and band gap energy, Diffuse Reflectance Spectroscopy UV-Vis (DRS-UV Vis SPECORD 210 Plus) was employed, while X-ray Photoelectron Spectroscopy (XPS: PHI-5702 multifunctional X-ray photoelectron spectrometer) measured the electron binding energies of the elements. Additionally, the pore size, surface area, and pore volume were determined using a Surface Area Analyzer (SAA: Quantachrome Nova 4200e). The quantity of reduced dye was quantified with a UV-Vis spectrophotometer (Thermo Scientific, Genesys 20), and the concentrations of adsorbed heavy metals were analyzed by Atomic Absorption Spectroscopy (AAS: AA240).

2.7. Photocatalytic activity determination of nanocomposites

The prior procedure was used to determine photocatalytic activity on the direct red 81 dye degradation (Rahmayeni et al., 2023). 10 mg of nanocomposites (CoZnHA1, CoZnHA2, CoZnHA3, and CoZnHA4) were added to 20 mL of a solution containing direct red 81 dye at a 30 mg/L concentration. After stirring, the resulting suspension was exposed to sunlight for 120 minutes, between 11:00 am and 1:00 pm. Following the irradiation, distilled water was added to restore the liquid to its initial volume. The suspension was then separated from the CoZnHA nanocomposite. Subsequently, aliquots were taken, and the absorbance was measured at 530 nm using a UV-Vis spectrophotometer. The photodegradation of the dye was measured by the following 4 equations:

$$D\ (\%) = \frac{A_0 - A_t}{A_0} x\ 100\% \quad (4)$$

where A_o is the initial absorbance of the dye solution and At is the dye solution at a time in mn (Mohammed et al., 2024). The effect of several significant parameters-including catalyst type, dye concentration (10–50 mg/L), exposure time duration (30–120 minutes), and catalyst loading (0–25 mg)—on the photodegradation process was also examined. After the initial reaction cycles, the photocatalyst was retrieved, and its reusability was assessed by comparing it to a fresh sample. Each experiment was repeated three times to test for repeatability.

2.8. Adsorption ability determination

The adsorption capacity of the synthesized samples for cadmium metal ions (Cd(II)) was evaluated using a modified version of the previous method (Sery et al., 2021). The nanocomposites selected for this assay are CoZnHA3 and CoZnHA4 due to their superior photocatalytic performance. Here's the procedure: a stock solution of Cd(II) was first prepared by dissolving 1 g of $CdCl_2 \cdot H_2O$ in distilled water in a 1000 mL volumetric flask, yielding a concentration of 1000 mg/L. Subsequently, cadmium ion solutions with concentrations of 20, 30, 40, and 50 mg/L were prepared by diluting the stock solution appropriately. The influence of initial concentration on the adsorption capacity of the nanocomposite was evaluated by adding 10 mg of the nanocomposites to Cd(II) solutions of varying concentrations and allowing them to stand for 30 minutes. Subsequently, the liquid phase was separated from the nanocomposite solid using centrifugation, and the remaining cadmium ions that were not adsorbed were quantified using atomic absorption spectroscopy (AAS). The adsorption percentage was determined by comparing the metal ion concentrations before and after the treatment process. Equation 5 was applied to calculate the adsorption percentage for the tested samples.

$$\text{Adsorption percentage} = \frac{C_0\text{-}C_t}{C_0} \text{ x } 100\% \quad (5)$$

where C_0 is the initial concentration, and C_t is the final concentration of the Cd(II) solution which is obtained using the Lambert Beer equation (Kartika et al., 2023). The effect of the exposure time on the nanocomposite's adsorption capacity was investigated by adjusting the contact time (30, 60, 90, and 120 minutes). Additionally, variations in the amount of CoZnHA3 and CoZnHA4 nanocomposites (10, 15, 20, and 25 mg) were conducted to study the effect of adsorbent quantity on adsorption ability.

3. Results and Discussion

3.1. Structure analysis by XRD

To determine the crystallization properties and phase composition of synthesized samples X-ray diffraction (XRD) is studied. Figure 1(a) displayed the XRD pattern of standard $ZnFe_2O_4$, synthesized $ZnFe_2O_4$, and $Co_{0.1}Zn_{0.9}Fe_2O_4$. The XRD pattern of the synthesized $ZnFe_2O_4$ sample exhibited the same pattern as ICSD standard #158837 with specific peaks at 2θ = 30.1˚, 35.7˚, 43.4˚, 53.7˚, 57.3˚ from the planes of (220), (311), (400), (422), and (511). The peaks were found to be well-defined, had a good distribution of nanoparticles and crystalline nature, and no impurities were observed. Meanwhile, the $Co_{0.1}Zn_{0.9}Fe_2O_4$ pattern exhibited the same pattern as synthesized $ZnFe_2O_4$ with a slight shift of the peaks towards a larger 2θ, indicating a decrease in the lattice volume due to the smaller lattice parameters. The changes in 2θ are expected due to the substitution of a larger ionic cation, Zn^{2+} (radius of 0.82 Å), by a smaller Co^{2+} cation (radius of 0.74 Å). Equation 6 is Scherer's equation was used to estimate the average crystallite size for nanocomposites:

$$D = k\lambda/\beta \cos\theta \quad (6)$$

where D represents the average crystallite size, λ denotes the wavelength of CuK radiation, β refers to the full width at half maximum (FWHM) of the diffraction peaks, θ is the Bragg angle, and K is the Scherrer constant. (Suryawanshi et al., 2023). The average crystal size of $Co_{0.1}Zn_{0.9}Fe_2O_4$ is 10.18 nm. The small crystal size of $Co_{0.1}Zn_{0.9}Fe_2O_4$ is caused by the synthesis process using a hydrothermal method at a fairly low temperature, so the crystal growth is not perfect. The synthesis of spinel ferrite $CoxZn1\text{-}xFe_2O_4$ by other researchers employed the co-precipitation method, yielding crystal sizes between 24 to 40 nm. These

larger crystal sizes, compared to those observed in this study, result from using the co-precipitation method followed by a high-temperature calcination process. Heating at elevated temperatures accelerates crystal growth by merging smaller crystals with identical orientations into larger ones (Asogekar and Verenkar, 2019).

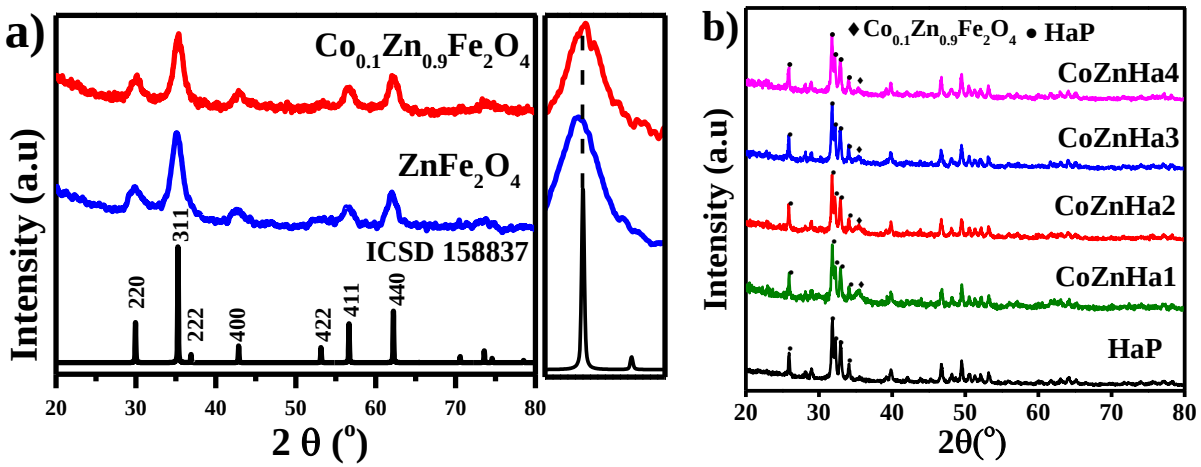

Figure 1 XRD a) patterns of standard $ZnFe_2O_4$, synthesized $ZnFe_2O_4$, and $Co_{0.1}Zn_{0.9}Fe_2O_4$, and b) composites

Figure 1(b) shows the XRD patterns of hydroxyapatite samples and the CoZnHA1, CoZnHA2, CoZnHA3, and CoZnHA4 nanocomposites. The diffractograms of the nanocomposite samples show distinctive peaks for both hydroxyapatite and $Co_{0.1}Zn_{0.9}Fe_2O_4$, confirming the formation of the nanocomposites. The XRD patterns of synthesized nanocomposite exhibit the dominant peaks of the hydroxyapatite phase and a single peak of the $Co_{0.1}Zn_{0.9}Fe_2O_4$ phase with a lower intensity indicating the presence of both phases in the nanocomposite samples. The specific diffraction peaks of $Co_{0.1}Zn_{0.9}Fe_2O_4$ were observed at 2θ = 35.9 with a Miller index (311), while the specific peaks of hydroxyapatite were observed at 2θ = 25.9°, 31.8°, 32.4°, 33.9°, 34.1°, 39.8°, 46.9°, and 49.5°. Furthermore, no other peaks of any impurities and secondary phases are observed. The peak height of the hydroxyapatite was not considerably impacted by the nanocomposite's increased mass of $Co_{0.1}Zn_{0.9}Fe_2O_4$.

3.2. Analysis by SEM-EDX

Figure 2 displayed the morphology of CoZnHA nanocomposite analyzed by SEM with a magnification of 20,000. The hydroxyapatite granules exhibit a relatively homogenous shape with slight agglomeration. The capping agent employed can affect the morphology forms. In this work, gambir leaf extract was used as a source of capping agent due to gambir leaf extract contains secondary metabolite compounds such as flavonoids, which can act as a capping agent. The presence of a capping agent in gambir leaf extract can minimize the occurrence of agglomeration (Wahyuni et al., 2019). Since spinel ferrite's magnetic characteristics attract each other to create larger clusters, adding more spinel ferrite results in a slightly agglomerated nanocomposite.

The components of the nanocomposite were examined using the EDX device. Figure S2 shows the EDX spectrum of CoZnHA, illustrating the elements present in the nanocomposite samples. The elements present in the CoZnHA nanocomposite, such as calcium (Ca), phosphate (P), and oxygen (O), which are constituent elements of hydroxyapatite, and cobalt (Co), iron (Fe), and zinc (Zn), which are constituent elements of $Co_{0.1}Zn_{0.9}Fe_2O_4$, are

indicated by the peaks that appear in the EDX spectrum. The CoZnHA nanocomposite contains a more significant Ca and P element composition than the pristine $Co_{0.1}Zn_{0.9}Fe_2O_4$ because hydroxyapatite is a matrix and exists in a greater quantity. The increase in the ferrite content in the nanocomposite is directly proportional to the height of the peaks representing the ferrite's constituent elements (Table 2).

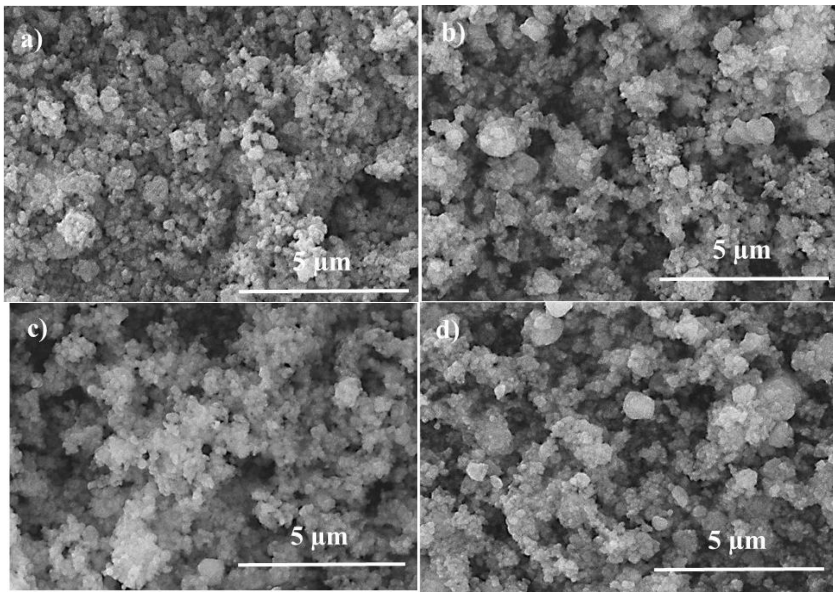

Figure 2 SEM images of a) CoZnHA1, b) CoZnHA2, c) CoZnHA3, and d) CoZnHA4 with a magnification of 20,000

Table 2 Composition of elements in the synthesized composites

Elements (%w)	CoZnHA1	CoZnHA2	CoZnHA3	CoZnHA4
Co	0.41	0.36	0.41	0.69
Fe	2.88	4.73	6.04	9.91
O	39.61	37.8	40.73	38.33
Zn	1.57	1.85	2.51	4.11
Ca	35.56	37.10	33.5	30.38
P	19.64	18.67	16.81	16.58

3.3. Analysis by TEM, HRTEM and SAED

A more detailed analysis of structure, particle shape, and crystallinity was carried out with TEM, HRTEM, and SAED (Figure 3). TEM image of $Co_{0.1}Zn_{0.9}Fe_2O_4$ (Figure 3a–b) illustrates the particles' morphology in the cube-like granular phase with diameters less than 50 nm. There is a slight agglomeration caused by the magnetic properties of the spinel ferrite in nanocomposites. Figure 3(c-d) illustrates the granular morphology of CoZnHA3 and CoZnHA4 nanocomposite particles, where $Co_{0.1}Zn_{0.9}Fe_2O_4$ ferrite spinel is encapsulated within hydroxyapatite. Figure 3e presents the HRTEM image of the CoZnHA4 nanocomposite, indicating that the combined components are on the nanoscale. The selected area electron diffraction (SAED) patterns shown in Figure 3f confirm the polycrystalline nature of the samples under investigation. The ring pattern is indexed to reflections corresponding to the Fd-3m space group. Moreover, the SAED patterns closely match the simulated patterns generated from ferrite crystal structure data. Compared to previous studies that used $CuFe_2O_4$ as the ferrite material, the nanocomposite particles produced in this study exhibit a more uniform and regular shape (Rahmayeni et al., 2023).

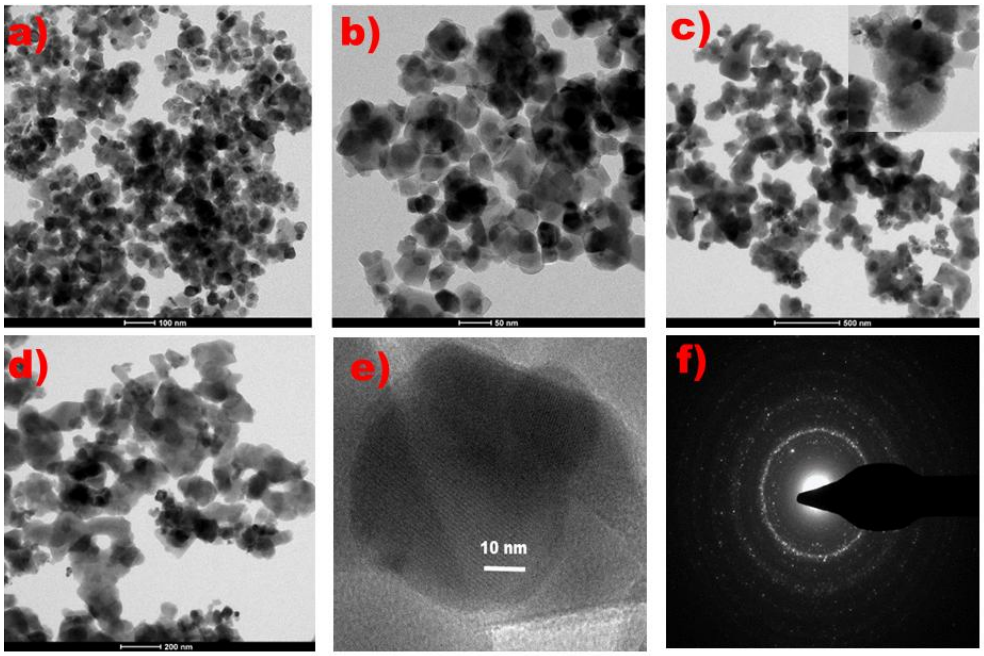

Figure 3 TEM images of $Co_{0.1}Zn_{0.9}Fe_2O_4$ with different magnifications (a-b), CoZnHA3 and CoZnHA4 nanocomposites (c-d), HRTEM image and SAED pattern of CoZnHA4 (e-f)

3.4. Analysis by FTIR

Fourier transform infrared (FTIR) spectroscopy was utilized to validate the spinel ferrite and hydroxyapatite structures in the prepared samples. Figure 4 represents the FTIR spectrum of prepared samples within the range from 400 to 2000 cm^{-1}. Figure 4a shows the band of hydroxyapatite and $Co_{0.1}Zn_{0.9}Fe_2O_4$.

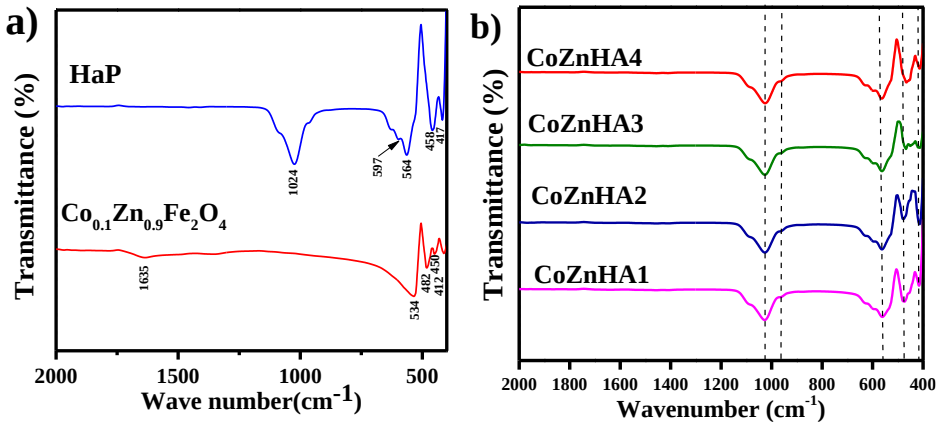

Figure 4 FT-IR spectra of $Co_{0.1}Zn_{0.9}Fe_2O_4$ and hydroxyapatite (a) and CoZnHA1, CoZnHA2 CoZnHA3, and CoZnHA4 (b).

The specific absorption band of $Co_{0.1}Zn_{0.9}Fe_2O_4$ appeared at a wave number of 482 cm^{-1}, which indicates the presence of M–O vibrations on the octahedral side of Fe-O/Co-O, while the absorption at a wave number of 534 cm^{-1} indicates the presence of M–O vibrations on the tetrahedral side of Zn-O/Co-O. The bands observed in this investigation are consistent with previous findings (Mohamed et al., 2019). Meanwhile, the spectrum of hydroxyapatite appeared at specific wave numbers of 564 cm^{-1} and 597 cm^{-1}, which indicates the antisymmetric vibration of the O-P-O bond from the PO_4^{3-} group (Sery et al., 2021).

Additionally, the FT-IR spectrum of the synthesized CoZnHA (1-4) nanocomposites is shown in Figure 4b. The absorption band at 1018 cm^{-1} corresponds to the PO_4^{3-} group from hydroxyapatite, while the band at 1628 cm^{-1} is attributed to the C=C group (alkene) from the betel leaf extract. Moreover, the absorption below 548 cm^{-1} indicates the Fe-O stretching vibration of the ferrite spinel in the nanocomposites (Cahyana et al., 2021).

3.5. Magnetic properties analysis by VSM

The magnetic properties of synthesized nanocomposites with different ratios of hydroxyapatite and $Co_{0.1}Zn_{0.9}Fe_2O_4$ were investigated using VSM equipment at room temperature, which is given in the form of a hysteresis curve, as shown in Figure 5A. The hysteresis curve indicates that the nanocomposite samples exhibit soft magnetic properties, as evidenced by the relatively low values of saturation magnetization (Ms), remanent magnetization (Mr), and coercivity (Hc) for nanocomposites, as presented in Table 3. The magnetic properties of the nanocomposites are attributed to $Co_{0.1}Zn_{0.9}Fe_2O_4$, as hydroxyapatite is not a magnetic material. Consequently, the magnetic properties of the nanocomposite enhance with the increasing amount of ferrite. According to Das et al. (2020), the small Ms value occurs due to the coating of non-magnetic materials, such as hydroxyapatite, on the magnetic material in the nanocomposites (Das et al., 2021).

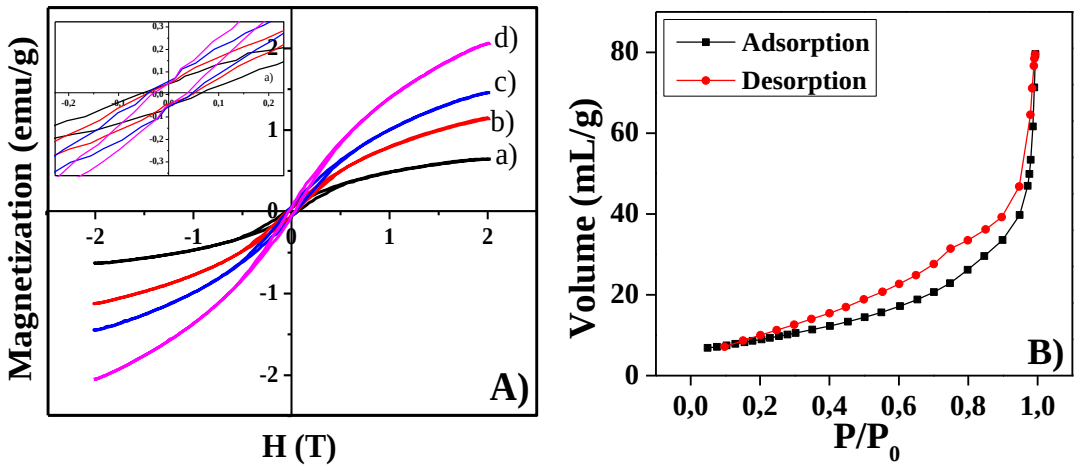

Figure 5 A)The hysteresis curve of a) CoZnHA1, b) CoZnHA2, c) CoZnHA3, d) CoZnHA4, and B) N_2 adsorption-desorption isotherm curve for CoZnHA4 sample

Table 3 Saturation magnetic (Ms), remanent magnetic (Mr), and coercivity (Hc) values of the synthesized nanocomposite samples.

Samples	Ms (emu/g)	Mr (emu/g)	Hc (Oe)	Mr/Ms
CoZnHA1	0.6424	0.0467	59.6	0.073
CoZnHA2	1.1365	0,0486	44.2	0.043
CoZnHA3	1.4587	0.0490	44.2	0.033
CoZnHA4	2.0681	0.0582	33.5	0.028

From the shape of the hysteresis curve, it can be concluded that the CoZnHA nanocomposites are superparamagnetic following the research results obtained by Gómez et al. (2018). The magnetic properties of the obtained nanocomposites are stronger than those obtained by (Das and Dhar, 2020) and (Rahmayeni et al., 2023) . The magnetic properties of nanocomposites are an advantage of the catalyst in a photocatalytic degradation process. These nanocomposites can be separated from the solution quickly and

easily with a permanent magnet after the degradation photocatalytic process and can be used for the next application (Ai et al., 2023).

3.6. Adsorption-desorption analysis by BET

Figure 5B shows the adsorption-desorption isotherm curve from the Brunauer-Emmett-Teller (BET) analysis for the CoZnHA4 nanocomposite. The curve indicates a gradual increase in relative pressure (P/P0) initially, but a rapid increase is observed at a relative pressure range of 0.6 to 1. The increase in P/P0 is due to the interaction of adsorbed gas molecules on the surface of the solid, forming a single layer (Kahrizi et al., 2018). The CoZnHA4 sample has an average pore diameter of 7.52 nm, placing it within the mesoporous category, as mesopores range from 2 to 50 nm. The specific surface area of the CoZnHA4 sample is 32.01 m^2/g, and its pore volume is 0.12 mL/g. The results obtained are broader than those reported in previous research (Ullah et al., 2023). As well known, the surface area significantly impacts a material's effectiveness as a photocatalyst and adsorbent. A larger surface area provides more active sites for interactions with dyes and metal ions, leading to higher activity.

3.7. Optical properties analysis by DRS-UV Vis

The optical properties of the nanocomposite samples were evaluated using DRS UV-Vis equipment. The Kubelka-Munk theory, which is commonly employed for analyzing optical band gap energy through diffuse reflectance, was utilized in this study (Paydar et al., 2020).

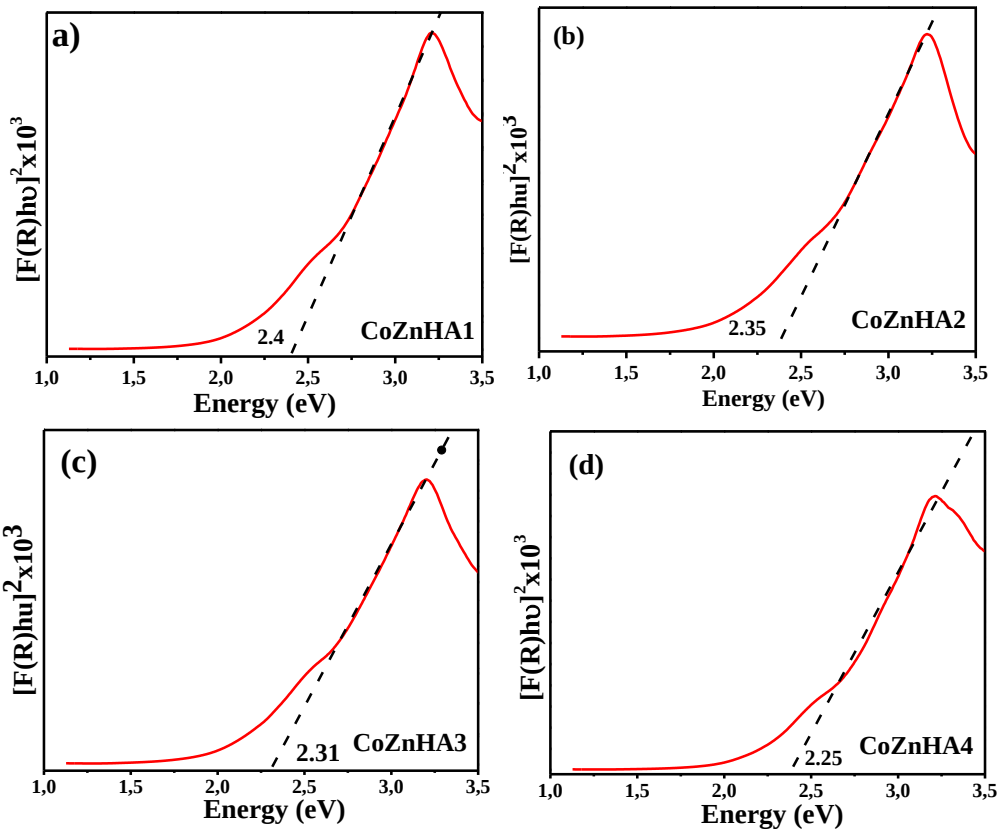

Figure 6 The Tauc Plot of CoZnHA1 (a), CoZnHA2 (b), CoZnHA3 (c), and CoZnHA4 (d) to estimate the energy gap obtained from DRS UV-vis measurements

Using the Tauc equation, the estimated band gap energy of each nanocomposite was 2.4, 2.35, 2.31, and 2.4 eV for the CoZnHA1, CoZnHA2, CoZnHA3, and CoZnHA4, respectively (Figure 6). The band gap variation depends on various factors such as crystallite size, crystallinity, lattice strain, structural parameters, and the presence of defects or impurities (Yadav et al., 2017). The increment of the optical band gap energies by increasing the $Co_{0.1}Zn_{0.9}Fe_2O_4$ proportion from 5 wt% to 20 wt% (decrement of the HA proportion from 95 wt% to 80 wt%). The band gap energy obtained indicates that the CoZnHA nanocomposite absorbs light in the visible light region, where in this study, sunlight was used as a light source (Das et al., 2021). This optical property is helpful in its application as a photocatalyst because sunlight can move its activity to degrade organic dyes more efficiently.

3.8. XPS study

X-ray photoelectron spectroscopy (XPS) was utilized to investigate the elemental composition and electron states of atoms in the material (Figure S3). The XPS spectrum provided comprehensive details on the surface composition and chemical states of all elements present in CoZnHA4. The high-resolution XPS spectra of CoZnHA4 (Figure S3a) and the spectra for O1s, Ca2p, P2p, C1s, Fe2p, Zn2p, and Co2p are displayed in Figures S3b–f. The XPS spectrum of O 1s indicates the presence of various oxygen species on the sample's surface. In Figure S3b, the peak at 527.7 eV ($O1s_3/_2$) is assigned to lattice oxygen (M–O–M) within the metal–oxygen framework, while the peak at 530 eV (O $2p_1/_2$) corresponds to oxygen atoms in the PO_4^{3-} group. The high-resolution XPS spectrum for Ca2p, depicted in Figure S3c, reveals two peaks with binding energies of 349.3 eV (Ca $2p_1/_2$) and 345.7 eV (Ca $2p_3/_2$).

The peak around 349.2 eV for Ca $2p_3/_2$ indicates that calcium atoms are bonded to phosphate groups (PO_4^{3-}). In Figure S3d, the P2p spectrum shows two peaks at binding energies of 131.6 eV (P $2p_1/_2$) and 132.1 eV (P $2p_3/_2$) within the nanocomposite. These binding energy values for P2p are lower than those typically found in pure hydroxyapatite (134.13 eV and 133.18 eV), suggesting an interaction with the $Co_{0.1}Zn_{0.9}Fe_2O_4$ nanoparticles (Das and Dhar, 2020). In the arrangement of oxygen atoms, Fe(II) is positioned at the octahedral site, while Fe(III) occupies the tetrahedral site. The deconvoluted iron peak reveals two primary peaks with binding energies of 709.04 eV and 723.36 eV, corresponding to $Fe2p_3/_2$ and $Fe2p_1/_2$, respectively (Figure S3e). The Zn 2p core-level spectra, shown in Figure S3f, display two fitting peaks at approximately 1018.7 eV and 1042 eV, which are attributed to Zn $2p_3/_2$ and Zn $2p_1/_2$, respectively (Hanamanta et al., 2023). The appearance of these element peaks indicates the formation of a hydroxyapatite/ $Co_{0.1}Zn_{0.9}Fe_2O_4$ nanocomposite. The C 1s peak observed at 283 eV is predicted to be the carbon used in the measurements (Figure S3h).

3.9. Photocatalytic activity

The photocatalytic activity of the nanocomposite was determined on the degradation of direct red 81 dye under direct solar light (Figure 7). To obtain the nanocomposites with higher activity, photocatalytic activity was determined for all nanocomposites using direct red 81 dye solution with the following conditions: the dye concentration is 20 mg/L, the amount of nanocomposite is 20 mg, and the exposure time is 2 h. From Figure 7a, it can be seen that without a catalyst (NC), the degradation percentage only reaches 28%. With a catalyst in the form of a composite, the degradation percentage increases above 80%. CoZnHA3 and CoZnHA4 nanocomposites exhibit better activity compared to the other nanocomposites. Therefore, CoZnHA3 and CoZnHA4 were utilized to determine the optimal

concentration and contact time. The efficiency test for direct red 81 dye concentration revealed a degradation percentage of 92.25% after 2 hours (Figure 7b). As the concentration increases, the degradation percentage obtained becomes lower. The decrease in degradation percentage with increasing dye concentration is due to the higher number of direct red 81 molecules in the liquid, which blocks sunlight from reaching the nanocomposite material. Consequently, OH· formation, which is crucial for the degradation process, is reduced. As is known, the OH radical is a group that plays an important role in breaking down dye compounds into CO_2 and H_2O (Kusdianto et al., 2020). This finding is consistent with the results reported by(Das and Dhar, 2020). In this photocatalytic process, the presence of hydroxyapatite in the composite can help spread the ferrite material so that agglomeration can be reduced and catalytic activity becomes better.

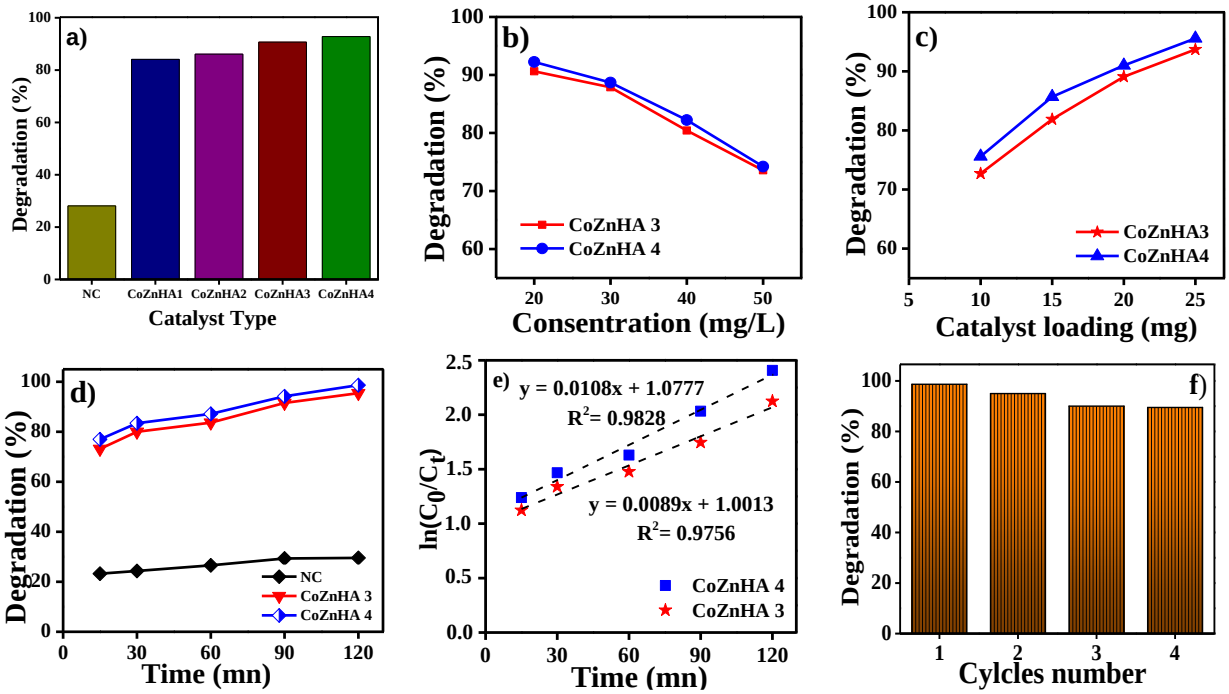

Figure 7 Photocatalytic activity of samples (a) with different concentrations of direct red 81 concentrations, (b) with different amounts of CoZnHA catalyst, (c) with different exposure times, (d) the reaction kinetics in the degradation of direct red 81 dye, and (f) recycles number.

Determination of the optimal dosages of the nanocomposites used as photocatalysts in the degradation of direct red 81 dye is represented in Figure 7c. The degradation percentage increases with the number of photocatalysts as more active sites become available for the degradation process. The optimal photocatalyst dosage is 25 mg, resulting in a degradation percentage of 95.57%. As reported by (Rahmayeni et al., 2022), increasing the amount of photocatalyst provides more active sites, leading to improved dye degradation. The best exposure contact time test for the CoZnHA nanocomposite on direct red 81 dye degradation is shown in Figure 7d. The optimal contact time was found to be 2 hours, with the degradation percentage reaching 98,65%. Rahmayeni et al.'s research indicates that the proportion of degradation increased with exposure duration. With the increasing contact time, the degradation efficiency increased because the number of OH· radicals formed increased (Rafiq et al., 2021; Rahmayeni et al., 2019).

The kinetic parameters were determined by plotting Ln(Ct/C0) against the reaction time. Figure 7e is the reaction kinetics curve in the photocatalysis process driven by sunlight. From the shape of the curve, it can be concluded that the kinetics of the degradation process follow the pseudo-first-order kinetic model (Hassaan et al., 2022). The recycling test of the CoZnHA4 nanocomposite was conducted by separating the photocatalyst after each cycle of exposure using centrifugation to recover the catalyst. The recovered catalyst was then washed with absolute alcohol, followed by deionized water. It was subsequently dried overnight in an oven at 70°C. After drying, the collected nano catalyst was reintroduced into a freshly prepared direct red 81 dye solution to begin the next experimental cycle (Figure 7f). In the first and second cycles, there was a slight decrease in degradation percentage. However, in cycles 3 and 4, the reduction in degradation percentage was not significant.

3.10. Adsorption ability determination of Cd(II) ion in water

The heavy metal Cd (II) in water was used to test the nanocomposite's capacity for adsorption (Figure 8). The effect of initial concentration on the removal of Cd (II) ions by CoZnHA3 and CoZnHA4 adsorbents was investigated at different initial concentrations ranging from 20 to 50 mg/L. Figure 8a presents the curve demonstrating the composite's capability to adsorb Cd (II) metal ions at various concentrations. Initially, the adsorption capacity increased with the rise in the initial dye concentration. This can be attributed to the fact that at lower initial concentrations, the adsorbent surface is more accessible. As the initial concentration of Cd (II) increases, the number of Cd (II) metal ions adsorbed also increases. However, once all active sites on the adsorbent are occupied, further increases in Cd (II) concentration result in a decrease in adsorption capacity due to the lack of available adsorption sites. The optimum metal ion concentration obtained was 20 mg/L with an adsorption percentage of 90.9 % and 92.51% for CoZnHA3 and CoZnHA4. According to Das K et al. (2020), increasing the concentration of Cd (II) ions will reduce the adsorption efficiency because the amount of adsorbent that remains is not proportional to the greater number of Cd (II) ions so that the adsorbent has reached a saturation point in its adsorption. Moreover, the saturation of the active site leads the dye molecules to release back into the solution due to the agitation (Rahmayeni et al., 2023; Das et all., 2020).

To investigate the impact of adsorbent quantity, 10 to 30 mg of the nanocomposite was used keeping the other parameters. The result showed that, at an initial metal concentration of 30 mg/L, the maximum removal percentage of Cd (II) for the adsorbent dosage of 25 mg was around 78.05% and 81.09% for CoZnHA3 and CoZnHA4. (Figure 8b). It was observed that when the number of nanocomposites employed grew, so did the adsorption efficiency because more active sites on the composite surface were available to adsorb Cd(II) metal ions (Nayak and Bhushan, 2021).

Furthermore, contact time also plays a role in adsorption efficiency. The time-dependent behavior of Cd (II) adsorption was assessed by varying the contact time between the adsorbate and adsorbent from 15 to 120 minutes, using an initial concentration of 30 mg/L and 25 mg of adsorbent. CoZnHA3 and CoZnHA4 nanocomposites were used for this study. The graph shows that the adsorption grew quickly during the first 60 mn before becoming slowly saturated at the 120-minute mark (Figure 8c). During the initial stage of adsorption, a larger number of active sites are available on the adsorbent. As the contact time increases, these active sites gradually become occupied, reducing the number of available sites. This results in a slower adsorption rate until equilibrium is eventually reached (Hassaan et al., 2022; Nayak and Bhushan, 2021). The optimum contact time for Cd

(II) metal ions adsorption is 120 mn with an adsorption percentage of 88.99%. The adsorption capacity for 2 hours was 97.3 mg/g for CoZnHA3 and 97.9 mg/g for CoZnHA3.

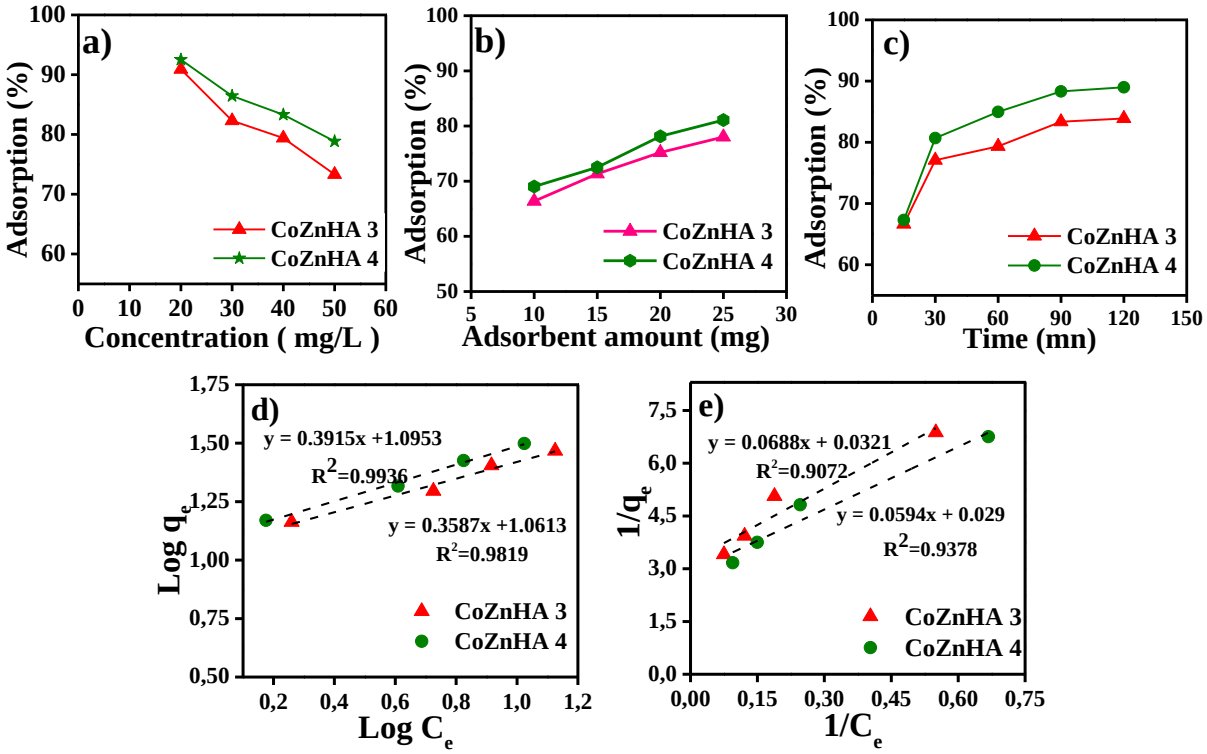

Figure 8 Test graph for nanocomposite adsorption capability (a) variation in the amount of CoZnHA adsorbent (b) variation in CoZnHA adsorption time, (c) variation in Cd(II) metal ion concentration, and (d) Freundlich isotherm curve, and (e) Langmuir isotherm curve of Cd(II) ion adsorption

Adsorption isotherms were evaluated using the Langmuir and Freundlich models. The Langmuir isotherm refers to an adsorption process that takes place chemically in a single layer (monolayer), while the Freundlich isotherm refers to a chemical adsorption process that involves many layers (multilayer). The linear form of the Langmuir and Freundlich equation can be expressed as 7 and 8 equations as follows:

$$\frac{C_e}{q_e} = \frac{C_e}{q_m} + \frac{1}{q_m K_L} \quad \text{Langmuir} \tag{7}$$

$$\ln q_e = \ln K_F + \frac{1}{n} \ln C_e \quad \text{Freundlich} \tag{8}$$

In this context, q_e (mg/g) represents the equilibrium concentration of metal ions, C_e (mg/L) denotes the equilibrium adsorption concentration for Cd(II), and q_m (mg/g) indicates the maximum adsorption capacity. K_L is the adsorption constant of the Langmuir model. The constants b and q_m can be determined from the slope and intercept of the linear plot of 1/qe versus 1/Ce . K_F represents the adsorption constant of the Freundlich model. n was the Freundlich isotherm exponent (Wang and Shih, 2021; Wang et al., 2019). The Freundlich isotherm was obtained by graphing Log Ce vs log qe (Figure 8d) and the Langmuir model on the equilibrium data was obtained by plots of 1/Ce versus 1/Qe (Figure 8e). The results of the isotherm analysis are summarized in Table 4. By comparing the coefficient of determination (R^2), it is evident that the Langmuir isotherm model was not suitable for this study. The adsorption kinetics of Cd(II) ions were found to follow the Freundlich isotherm

model, with R^2 values of 0.9936 for CoZnHA3 and 0.9819 for CoZnHA4. The maximum capacity obtained from the Langmuir isotherm using CoZnHA 4 adsorbent is 97.9 mg/g. The maximum capacity obtained in this study was lower than the results obtained by several previous studies (Table 5). This difference may be due to the smaller amount of adsorbent used, variations in experimental conditions, and differences in the type of adsorbent.

Table 4 Langmuir and Freundlich isotherm coefficients for the adsorption of Cd (II) ion

Adsorbent	Langmuir isotherm			Freundlich isotherm		
	K_L (L/mg)	Q_m (mg/g)	R^2	K_F	n	R^2
CoZnHA 3	0.46	97.3	0.9072	1.077	14.53	0.9936
CoZnHA 4	0.49	97.9	0.9378	1.069	16.84	0.9819

Table 5 Maximum adsorption capacity of different adsorbents for Cd(II) ions removal

Material	Capacity (mg/g)	References
$NiFe_2O_4$/HAp/graphene	344.83	(Kahrizi et al., 2018)
Magnetic ferrite	160	(Liu et al., 2018)
HAP/$ZnFe_2O_4$	107	(Das and Dhar, 2020)
$xZnO_{(1-x)}Fe_2O_4$	82.45	(Khezami et al., 2017)
Hydroxyapatite/$Co_{0.1}Zn_{0.9}Fe_2O_4$	97.9	This work

4. Conclusion

Magnetic hydroxyapatite/$Co_{0.1}Zn_{0.9}Fe_2O_4$ nanocomposites were successfully synthesized using Pensi clam shells as a source of CaO, which was then utilized to prepare hydroxyapatite. X-ray analysis reveals that the nanocomposites exhibit good crystallinity without impurities. Absorption bands at wave numbers 482 and 534 cm^{-1} indicated the presence of octahedral and tetrahedral sites of spinel ferrite in the nanocomposite. The magnetic properties of the samples increase with decreasing amounts of hydroxyapatite and growing quantities of spinel ferrite in the composite, as shown by the magnetic saturation value. HA/$Co_{0.1}Zn_{0.9}Fe_2O_4$ nanocomposites present an efficient and environmentally friendly method for removing heavy metals and dyes from wastewater. Under optimal conditions, the catalytic activity of the nanocomposite achieved 98.65% degradation of direct red 81 dyes after two hours driven by sunlight irradiation. It removed 92.51% of Cd (II) ions from the aqueous solution. The maximum capacity obtained from the Langmuir isotherm using CoZnHA 4 adsorbent is 97.9 mg/g. Furthermore, the nanocomposite exhibits sufficient magnetic strength, enabling its easy isolation from the reaction mixture using an external magnet. Therefore, it can be concluded that the nanocomposites function as magnetically separable and highly recyclable catalysts for the degradation of pollutant dyes and metal ions in contaminated water.

Acknowledgments

We express our gratitude to the Ministry of Education, Culture, Research, and Technology of the Republic of Indonesia for funding this research under Research Contract Number DRTPM: 012/E5/PG.02.00.PL/2023, and Unand: T/15/UN16.19/PT.01.03/ PDUPT-Material Maju/2023.

Conflict of interests

The authors declare that they have no competing interests.

References

Ai, J., Shuai, Y., Hu, M., Cheng, L., Luo, S., Li, W., Chen, Z., Hu, L., Zhou, Z., 2023. Microstructural evolution and catalytic properties of novel high-entropy spinel ferrites MFe_2O_4 (M= Mg, Co, Ni, Cu, Zn). Ceram. Int. 49, 22941–22951. https://doi.org/10.1016/j.ceramint.2023.04.119

Asogekar, P.A., Verenkar, V.M.S., 2019. Structural and magnetic properties of nanosized $Co_xZn_{(1-x)}Fe_2O_4$ (x= 0.0, 0.5, 1.0) synthesized via autocatalytic thermal decomposition of hydrazinated cobalt zinc ferrous succinate. Ceram. Int. 45, 21793–21803. https://doi.org/10.1016/j.ceramint.2019.07.182

Cahyana, A.H., Liandi, A.R., Yulizar, Y., Romdoni, Y., Wendari, T.P., 2021. Green synthesis of $CuFe_2O_4$ nanoparticles mediated by *Morus alba* L. leaf extract: Crystal structure, grain morphology, particle size, magnetic and catalytic properties in Mannich reaction. Ceram. Int. 47, 21373–21380. https://doi.org/10.1016/j.ceramint.2021.04.146

Das, Krishna Chandra, Dhar, S.S., 2020. Removal of cadmium(II) from aqueous solution by hydroxyapatite-encapsulated zinc ferrite (HAP/$ZnFe_2O_4$) nanocomposite: kinetics and isotherm study. Environ. Sci. Pollut. Res. 27, 37977–37988. https://doi.org/10.1007/s11356-020-09832-8

Das, Krishna Ch, Dhar, S.S., 2020. Remarkable catalytic degradation of malachite green by zinc supported on hydroxyapatite encapsulated magnesium ferrite (Zn/HAP/$MgFe_2O_4$) magnetic novel nanocomposite. J. Mater. Sci. 55, 4592–4606. https://doi.org/10.1007/s10853-019-04294-x

Das, K.C., Dhar, S.S., Thakurata, D.G., Das, J., 2021. Sn(II) inserted on hydroxyapatite encapsulated nickel ferrite ($NiFe_2O_4$@HAp-Sn^{2+}): A novel nanocomposite for the effective photo-degradation of rhodamine B dye. J. Clean. Prod. 290, 1–12. https://doi.org/10.1016/j.jclepro.2020.125172

Dehghani, M., Ahmadi, B., Zonnoon, Y., Nourozi, E., Shamsedini, N., 2018. Decolorization of Direct Red 81 in Aqueous Solutions by Fenton Oxidation Process : Effect of System Parameters. Iran. J. Heal. Saf. Environ. 6, 1297–1302.

Desalegn, Y.M., Andoshe, D.M., Desissa, T.D., 2020. Composite of bentonite/$CoFe_2O_4$/hydroxyapatite for adsorption of Pb (II). Mater. Res. Express 7. https://doi.org/10.1088/2053-1591/abc71f

Elgarahy, A.M., Elwakeel, K.Z., Mohammad, S.H., Elshoubaky, G.A., 2021. A critical review of biosorption of dyes, heavy metals and metalloids from wastewater as an efficient and green process. Clean. Eng. Technol. 4, 100209. https://doi.org/10.1016/j.clet.2021.100209

Fatah, A.F.M.A., Mohamad, A.A., Ali, S.A.M., Muchtar, A., Arifin, N.A., Wan Yusoff, W.N.A., Hamid, N.A., 2023. Influence of ZnO on Electrochemical and Physiochemical Properties of Lanthanum Strontium Cobalt Ferrite as Cathode for Intermediate Temperature Solid Oxide Fuel Cells. Int. J. Technol. 14, 1123–1133. https://doi.org/10.14716/ijtech.v14i5.6341

Ganesan, M., Ganapathi, B., Govindasamy, P., 2024. Results in Chemistry $CoFe_2O_4$/rGO nanocomposite : Synthesis and enhanced ammonia gas sensing properties at room temperature. Results Chem. J. 7, 2–7. https://doi.org/doi.org/10.1016/j.rechem.2024.101342

Gómez-Polo, C., Recarte, V., Cervera, L., Beato-López, J.J., López-García, J., Rodríguez-Velamazán, J.A., Ugarte, M.D., Mendonça, E.C., Duque, J.G.S., 2018. Tailoring the structural and magnetic properties of Co-Zn nanosized ferrites for hyperthermia applications, Journal of Magnetism and Magnetic Materials. 465, 211-219.

https://doi.org/10.1016/j.jmmm.2018.05.051
Hanamanta, Matteppanavar, S., Hegde, B.G., 2023. Magnetic and electrical investigations of low dimensional $Co_{0.5}Zn_{0.5-x}CuxFe_2O_4$ nano ferrites. J. Alloys Compd. 954, 170031. https://doi.org/10.1016/j.jallcom.2023.170031
Handayani, T., Emriadi, Deswati, Ramadhani, P., Zein, R., 2024. Modelling studies of methylene blue dye removal using activated corn husk waste: Isotherm, kinetic and thermodynamic evaluation. South African J. Chem. Eng. 47, 15–27. https://doi.org/10.1016/j.sajce.2023.10.003
Hassaan, M.A., El Nemr, A., El-Zahhar, A.A., Idris, A.M., Alghamdi, M.M., Sahlabji, T., Said, T.O., 2022. Degradation mechanism of Direct Red 23 dye by advanced oxidation processes: a comparative study. Toxin Rev. 41, 38–47. https://doi.org/10.1080/15569543.2020.1827431
Hernández-Origel, C.D., Patiño-Saldivar, L., Salazar-Hernández, M., Ardila, A.N., Talavera-López, A., Hernánez-Soto, R., Hernández, J.A., 2022. Use of Eichhornia Crassipes as a Bioadsorbent for the Removal of Methyl Orange and Methylene Blue Present in Residual Solutions. J. Ecol. Eng. 23, 193–211. https://doi.org/10.12911/22998993/151916
Ibrahim, M., Labaki, M., Giraudon, J.M., Lamonier, J.F., 2020. Hydroxyapatite, a multifunctional material for air, water and soil pollution control: A review. J. Hazard. Mater. 383, 121139. https://doi.org/10.1016/j.jhazmat.2019.121139
Javed, R., Zia, M., Naz, S., Aisida, S.O., Ain, N. ul, Ao, Q., 2020. Role of capping agents in the application of nanoparticles in biomedicine and environmental remediation: recent trends and future prospects. J. Nanobiotechnology. 18:172, 1-15. https://doi.org/10.1186/s12951-020-00704-4
Kahrizi, P., Mohseni-Shahri, F.S., Moeinpour, F., 2018. Adsorptive removal of cadmium from aqueous solutions using $NiFe_2O_4$/hydroxyapatite/graphene quantum dots as a novel nano-adsorbent. J. Nanostructure Chem. 8, 441–452. https://doi.org/10.1007/s40097-018-0284-3
Karamah, E.F., Anindita, L., Amelia, D., Kusrini, E., Bismo, S., 2019. Tofu industrial wastewater treatment with ozonation and the adsorption method using natural zeolite. Int. J. Technol. 10, 1498–1504. https://doi.org/10.14716/ijtech.v10i8.3471
Kartika, R., Ritonga, A.H., Sulastri, L., Nurnila, S., Irawan, D., Simanjuntak, P., 2023. Biosorption of Hexavalent Chromium Cr(VI) using *Microalgae Scenedesmus* sp as Environmental Bioindicator. Int. J. Technol. 14, 791–799. https://doi.org/10.14716/ijtech.v14i4.5188
Khezami, L., Taha, K.K., Ouldm'Hamed, M., Lemine, O.M., 2017. $_{(x)}ZnO_{(1\ x)}Fe_2O_3$ nanocrystallines for the removal of cadmium(II) and nickel(II) from water: kinetic and adsorption studies. J. Water Supply Res. Technol. - AQUA 66, 381–391. https://doi.org/10.2166/aqua.2017.033
Kusdianto, K., Widiyastuti, W., Shimada, M., Nurtono, T., Machmudah, S., Winardi, S., 2019. Photocatalytic activity of ZnO-Ag nanocomposites prepared by a one-step process using flame pyrolysis. Int. J. Technol. 10, 571–581. https://doi.org/10.14716/ijtech.v10i3.2902
Labanni, A., Zulhadjri, Handayani, D., Ohya, Y., Arief, S., 2020. Size controlled synthesis of well-distributed nano-silver on hydroxyapatite using alkanolamine compounds. Ceram. Int. 46, 5850–5855. https://doi.org/10.1016/j.ceramint.2019.11.035
Labanni, A., Zulhadjri, Z., Handayani, D., Ohya, Y., Arief, S., 2019. The effect of monoethanolamine as stabilizing agent in *Uncaria gambir* Roxb. mediated synthesis of silver nanoparticles and its antibacterial activity. J. Dispers. Sci. Technol. 0, 1–8.

https://doi.org/10.1080/01932691.2019.1626249

Lei, T., Li, S.J., Jiang, F., Ren, Z.X., Wang, L.L., Yang, X.J., Tang, L.H., Wang, S.X., 2019. Adsorption of Cadmium Ions from an Aqueous Solution on a Highly Stable Dopamine-Modified Magnetic Nano-Adsorbent. Nanoscale Res. Lett. 14, 1–17. https://doi.org/10.1186/s11671-019-3154-0

Liu, F., Zhou, K., Chen, Q., Wang, A., Chen, W., 2018. Comparative study on the synthesis of magnetic ferrite adsorbent for the removal of Cd(II) from wastewater. Adsorpt. Sci. Technol. 36, 1456–1469. https://doi.org/10.1177/0263617418779729

Madkhali, N., Prasad, C., Malkappa, K., Choi, H.Y., Govinda, V., Bahadur, I., Abumousa, R.A., 2023. Recent update on photocatalytic degradation of pollutants in waste water using TiO_2-based heterostructured materials. Results Eng. https://doi.org/10.1016/j.rineng.2023.100920

Mohamed, W.S., Alzaid, M., Abdelbaky, M.S.M., Amghouz, Z., García-Granda, S., Abu-Dief, A.M., 2019. Impact of CO^{2+} substitution on microstructure and magnetic properties of $Co_xZn_{1-x}Fe_2O_4$ nanoparticles. Nanomaterials 9, 1–17. https://doi.org/10.3390/nano9111602

Mohammed, N.A.H., Shamma, R.N., Elagroudy, S., Adewuyi, A., 2024. Chitosan incorporated nickel ferrite photocatalyst for complete photocatalytic degradation of ciprofloxacin, ampicillin and erythromycin in water. Results Chem. 7, 101307. https://doi.org/10.1016/j.rechem.2024.101307

Nayak, A., Bhushan, B., 2021. Hydroxyapatite as an advanced adsorbent for removal of heavy metal ions from water: Focus on its applications and limitations. Mater. Today Proc. 46, 11029–11034. https://doi.org/10.1016/j.matpr.2021.02.149

Padhan, A.M., Nayak, S., Sahu, M., Jagličić, Z., Koželj, P., Kim, H.J., 2023. Cationic redistribution induced magnetic properties of Zn^{2+} substituted $MgFe_2O_4$ spinel ferrite. Phys. B Phys. Condens. Matter 668, 415245. https://doi.org/10.1016/j.physb.2023.415245

Panda, S., Biswas, C.K., Paul, S., 2021. A comprehensive review on the preparation and application of calcium hydroxyapatite: A special focus on atomic doping methods for bone tissue engineering. Ceram. Int. 47, 28122–28144. https://doi.org/10.1016/j.ceramint.2021.07.100

Paydar, S., Akbar, N., Shi, Q., Wu, Y., 2020. Developing cuprospinel $CuFe_2O_4$–ZnO semiconductor heterostructure as a proton conducting electrolyte for advanced fuel cells. Int. J. Hydrogen Energy 1–11. https://doi.org/10.1016/j.ijhydene.2020.04.198

Rafiq, A., Ikram, M., Ali, S., Niaz, F., Khan, M., Khan, Q., Maqbool, M., 2021. Photocatalytic degradation of dyes using semiconductor photocatalysts to clean industrial water pollution Asma. J. Ind. Eng. Chem. 97, 111-128. https://doi.org/10.1016/j.jiec.2021.02.017

Rahmayeni, Azizah, N., Stiadi, Y., Putri, Y.E., Zulhadjri, 2022. Magnetic Particles Nanorod of ZnO/$CuFe_2O_4$ Prepared by Green Synthesized Approach: Structural, Optical and Magnetic Properties, and Photocatalytic Activity. Mater. Res. 25, 1–11. https://doi.org/10.1590/1980-5373-MR-2021-0164

Rahmayeni, Febrialita, R., Stiadi, Y., Putri, Y.E., Sofyan, N., Zulhadjri, 2021. Simbang Darah (*Iresine herbstii*) extract mediated hydrothermal method in the synthesis of zinc ferrite spinel nanoparticles used for photocatalysis and antibacterial applications. J. Environ. Chem. Eng. 9, 2, 105140. https://doi.org/10.1016/j.jece.2021.105140

Rahmayeni, Putri, J., Stiadi, Y., Zilfa, Zulhadjri, 2019. Green synthesis of $NiFe_2O_4$ spinel ferrites magnetic in the presence of *Hibiscus rosa-sinensis* leaves extract: Morphology, structure and activity. Rasayan J. Chem. 12, 1942–1949.

https://doi.org/10.31788/RJC.2019.1245304

Rahmayeni, Wendari, T.P., Ramadani, S., Stiadi, Y., Sofyan, N., Zulhadjri, 2023. $CuFe_2O_4$/hydroxyapatite magnetic nanocomposite synthesized using Pensi clam shells as a source of calcium for degradation of dye and anti-bacterial applications. Case Stud. Chem. Environ. Eng. 8, 1–10. https://doi.org/10.1016/j.cscee.2023.100482

Rimus, A., Hartati, W., Herry, A., Fathoni, A., Wendari, P., 2024. Bioresource Technology Reports Transforming seafood waste : Green mussel shell-derived hydroxyapatite as a catalyst for spirooxindole synthesis. Bioresour. Technol. Reports 25, 101796. https://doi.org/10.1016/j.biteb.2024.101796

Sery, A.A., El-Boraey, H.A., Abo-Elenein, S.A., ElKorashey, R.M., 2021. $CuFe_2O_4$@ hydroxyapatite composite for the environmental remediation of some heavy metal ions: Synthesis and characterization. Water Sci. 35, 154–164. https://doi.org/10.1080/23570008.2021.1994242

Supriyono, Kartikowati, C.W., Poerwadi, B., Wulandari, C., Hikma, L.L.F., Azzahra, A., Ghanyysyafira, K., Pinastika, H.L., 2023. The Formation Process of Hydroxyapatite Nanoparticles by Electrolysis and Their Physical Characteristics. Int. J. Technol. 14, 330–338. https://doi.org/10.14716/ijtech.v14i2.4452

Suryawanshi, S.M., Chandekar, K. V., Badwaik, D.S., Warhate, V. V., Gahane, N.M., Daf, S.R., 2023. Structural, surface, magnetic, and dielectric properties of $Ni_{0.3}Cu_{0.3}Zn_{0.4}Fe_{1.4}Cr_{0.6}O_4$ spinel ferrite nanocrystals prepared by sol-gel auto combustion route. Inorg. Chem. Commun. 156, 111204. https://doi.org/10.1016/j.inoche.2023.111204

Tamjidi, S., Esmaeili, H., Kamyab Moghadas, B., 2019. Application of magnetic adsorbents for removal of heavy metals from wastewater: A review study. Mater. Res. Express 6, 1–16. https://doi.org/10.1088/2053-1591/ab3ffb

Ubando, A.T., Africa, A.D.M., Maniquiz-Redillas, M.C., Culaba, A.B., Chen, W.H., Chang, J.S., 2021. Microalgal biosorption of heavy metals: A comprehensive bibliometric review. J. Hazard. Mater. 402, 123431. https://doi.org/10.1016/j.jhazmat.2020.123431

Ullah, R., Khitab, F., Gul, H., Khattak, R., Ihsan, J., Khan, M., Khan, A., Vincevica-Gaile, Z., Aouissi, H.A., 2023. Superparamagnetic Zinc Ferrite Nanoparticles as Visible-Light Active Photocatalyst for Efficient Degradation of Selected Textile Dye in Water. Catalysts 13, 1061. https://doi.org/10.3390/catal13071061

Wahyuni, S., Syukri, S., Arief, S., 2019. Green synthesis of Ag/TiO_2 Nanocomposite Assisted by Gambier Leaf (*Uncaria gambir* Roxb) Extract. J. Kim. Sains dan Apl. 22, 250–255. https://doi.org/10.14710/jksa.22.6.250-255

Wang, E.R., Shih, K.Y., 2021. Facile microwave hydrothermal synthesis of $ZnFe_2O_4$/rGO nanocomposites and their ultra-fast adsorption of methylene blue dye. Materials (Basel). 14, 1–22. https://doi.org/10.3390/ma14185394

Wang, M., Zhang, K., Wu, M., Wu, Q., Liu, J., Yang, J., Zhang, J., 2019. Unexpectedly High Adsorption Capacity of Esterified Hydroxyapatite for Heavy Metal Removal. Langmuir 35, 16111–16119. https://doi.org/10.1021/acs.langmuir.9b02373

Yadav, R.S., Kuřitka, I., Vilcakova, J., Urbánek, P., Machovsky, M., Masař, M., Holek, M., 2017. Structural, magnetic, optical, dielectric, electrical and modulus spectroscopic characteristics of $ZnFe_2O_4$ spinel ferrite nanoparticles synthesized via honey-mediated sol-gel combustion method. J. Phys. Chem. Solids 110, 87–99. https://doi.org/10.1016/j.jpcs.2017.05.029

Yue, X., Huang, J., Jiang, F., Lin, H., Chen, Y., 2019. Synthesis and characterization of cellulose-based adsorbent for removal of anionic and cationic dyes. J. Eng. Fiber. Fabr. 14, 1–10. https://doi.org/10.1177/1558925019828194